Received: 14 April 2018 | Revised: 17 May 2019 | Accepted: 6 June 2019
DOI: 10.1002/jrs.5659

RESEARCH ARTICLE

WILEY Journal of RAMAN SPECTROSCOPY

Raman measurements using a field-widened spatial heterodyne Raman spectrometer

Jun Qiu[1,2] | Xiangdong Qi[1] | Xiaotian Li[1] | Wenhui Xu[3] | Meihong Zhao[1,2] | Yuguo Tang[1] | Yixue Cheng[4] | Wenhao Li[1] | Jirigalantu[1] | Bayinheshig[1]

[1] Changchun Institute of Optics, Fine Mechanics and Physics, Chinese Academy of Sciences, Changchun, China

[2] University of Chinese Academy of Sciences, Beijing, China

[3] Department of Electrical and Electronic Engineering, Southern University of Science and Technology, Shenzhen, China

[4] School of Electronic Information, Wuhan University, Wuhan, China

Correspondence
Xiangdong Qi and Xiantian Li, Changchun Institute of Optics, Fine Mechanics and Physics, Chinese Academy of Sciences, Changchun, Jilin 130033, China.
Emails: chinagrating@263.net; lixt_1981@163.com

Funding information
Jilin Province Science and Technology Development Program Project in China, Grant/Award Number: 20190302047GX; National Natural Science Foundation of China (NSFC), Grant/Award Number: 61505204; National Major Scientific Instrument and Equipment Development Projects, Grant/Award Number: 2014YQ120351; Chinese Ministry of National Science and Technology, Grant/Award Number: 2014CB049500

Abstract

Spatial heterodyne Raman spectroscopy has become a useful spectroscopic detection technique that is particularly suitable for Raman measurements. This method uses the Fourier transform of the interferogram imaged on the detector by stationary diffraction gratings. Spatial heterodyne Raman spectroscopy has the same characteristic of conventional Fourier-transform spectroscopy, which is that the field of view is limited. We propose a two-dimensional spatial heterodyne Raman spectrometer (SHRS) that uses a field widening prism to effectively increase the throughput or sensitivity without sacrificing the spectral resolution for Raman measurements while broadening the bandpass. The signal-to-noise ratio is measured under different integrations or laser powers and shows that the system exhibits good stability and fair repeatability. Raman spectra obtained from the field-widened SHRS and a commercialized Raman instrument are compared, and the field-widened SHRS and the SHRS using the same instrumental parameters without field widening are also compared. A higher signal-to-noise ratio can be achieved using the field-widened SHRS. In our measurements, the field-widened SHRS can be operated under the slightly more complex conditions required for wide-field measurements with short integration times and low laser power. Raman spectra of a pure inorganic target or a target contained in glass and a plastic bottle are observed. A sulfate is investigated in two states: solid salt and aqueous solution. Several mixture liquids, mixture solids, minerals, and anti-Stokes Raman shifts are also investigated. The results show that the field-widened SHRS exhibits a good performance to successfully perform wide-field Raman measurements.

KEYWORDS
Raman spectroscopy, spatial heterodyne spectrometer, field widening, Fourier transform

1 | INTRODUCTION

Raman spectroscopy can provide detailed information about the vibrational and rotational energy levels of a molecule through inelastic scattering. It is a popular method and technique for identification and analysis because it is nondestructive, requires no sample preparation, and both organic and inorganic substances can be measured in various states. Owing to these advantages, Raman spectroscopy has already been applied in a variety

---

Xiangdong Qi and Xiaotian Li contributed equally to this work.

of fields, including physics,[1,2] chemistry,[3,4] biology,[5,6] medicine,[7,8] geology,[9,10] and electronics.[11] A spatial heterodyne Raman spectrometer (SHRS) possesses the multiple advantages, a larger entrance or higher light throughput than that a dispersion system, high spectral resolution, a compact, and rugged package without moving parts, and is compatible with a pulsed laser and gated detectors under ambient light conditions.[12] All these characteristics together make the SHRS very suitable for Raman measurements.

Spatial heterodyne Raman spectroscopy has been proven to be a very promising and useful technique for Raman experiments. Lamsal et al. reported that the SHRS can be used for wide-area Raman measurements with low laser irradiance in the deep UV[13] and standoff Raman measurements in the UV[14] that are free from longer wavelength fluorescence. However, the signal-to-noise ratio (SNR) of the SHRS is limited by the poor fringe visibility, and sample degradation is often observed when the laser is more tightly focused. Although Hu et al. have shown that the SHRS has the ability to obtain Raman spectra of targets in containers,[15] chemical warfare agents, and for simulant analysis,[16] which suffer from a serious fluorescence background, the SNR is not high so a long integration time and a larger laser power are usually needed. Foster et al. developed an SHRS that was designed to be fiber coupled for transmission-Raman observations to test paracetamol tablet samples. However, the non-filed-widening SHS was limited by the fiber diameter because the larger diameter produces a larger range of angles through the SHS.[17] Field widening is needed to increase the useable field of view without sacrificing the resolving power. This allows larger fiber diameters to be used. Conventional spatial heterodyne Raman spectroscopy has the same limited field of view (FoV) as that associated with Fourier transform spectroscopy. Usually, the performance of a conventional SHRS could be affected by the limited FoV, so that SNR is limited. Therefore, a long integration time and a larger laser power are used to improve the SNR, but this results in a strong laser irradiance that may damage the highly absorbing photosensitive or thermosensitive samples. To meet the measurement requirements of a larger and wider area, greater sensitivity, and shorter time, a 2-D SHRS offers field widening and achieves a doubling of the bandpass compared with that of a traditional one-dimensional SHRS without loss of spectral resolution. The field-widened SHRS requires no complex scanning or control mechanisms and has no moving parts owing to the incorporation of the prisms into the system. And, the field-widened SHRS largely enhances the FoV compared with that of a dispersion system. The increase FoV can be used to improve the sensitivity of the instrument and provide a wider area of coverage where a larger laser spot size or defocused excitation is beneficial to avoid sample photodegradation and thermal degradation.

Harlander et al. developed a field-widened SHS for observations of diffuse interstellar medium and proposed a new data reduction technique to correct the instrumental distortions resulting from optical defects, which paved the way for space applications by field-widened SHS.[18] Gardner et al. designed a high-resolution field-widened SHS to observe geocoronal Balmer α emission. The results of field-widened SHS showed excellent agreement with the already established Fabry–Perot interferometer observations.[19] Pannell et al. investigated a field-widened SHS in terms of its fundamental spectral resolution and its sensitivity, which achieved a S/N ration of unity with an input power of tens of femto-watts. It has concluded that the field-widened SHS could be tailored to making measurements of Raman spectra.[20] However, only spectra were obtained with a monochromatic source or calibration lamp, and no practical experiments for Raman spectra were conducted.

In this paper, we describe the design and performance of a field-widened SHRS. The field-widened SHRS is based on a stationary diffraction grating interferometer where selected prisms have been placed in the arms of the device. In our present work, the groove density of the diffraction gratings was 150 groove/mm, which is the same as the groove density of gratings used by Hu et al. and Foster et al. However, it requires lower laser powers and shorter integration times than those used by Hu et al.[15,16] and Foster et al.[17] The fundamental principles of field-widened SHRS are provided in Section 2. Then, the calibration results are reported in Section 3. In Section 4, SNR of the field-widened SHRS and the SHRS with the same instrumental parameters without field widening are compared. Further, we analyze the Raman results of the targets contained in glass or a plastic bottle, a mixture of organic liquids and inorganic solids, a sulfate in two states (solid salt and aqueous solution), rock-forming minerals, and anti-Stokes bands in detail.

2 | THEORETICAL

2.1 | Basic theory

The field-widened SHRS is depicted in Fig. 1. The laser beam, after passing through the linear variable filter and the clean-up filter, is split into two beams using beam splitter 1. After being reflected by mirror 1, such that the angle between the laser and the 532-nm razor edge dichroic was 45°, the excitation light was then focused

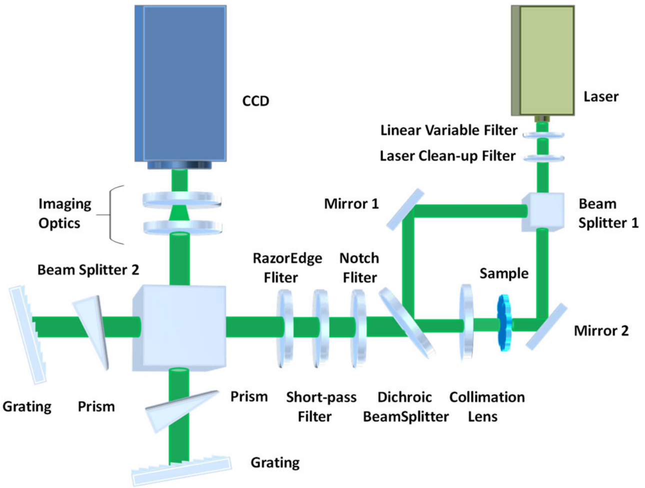

FIGURE 1 The field-widened spatial heterodyne Raman spectrometer system layout for Raman measurement [Colour figure can be viewed at wileyonlinelibrary.com]

on the sample. Mirror 2 is used to set the beam so that it was parallel to the optical axis. The scattered light is collimated by using the collimation lens, and the Rayleigh scattered light was filtered using a Raman edge filter or a notch filter. Collimated transmission light enters the field-widened SHRS and is incident on the beam splitter, which transmits and reflects 50 % of the incident radiation down the two arms of the interferometer respectively. The light is then incident on the gratings. The gratings are tilted at a fixed Littrow angle to the optical axis so that light at the Littrow wavelength exits the interferometer parallel to the optical axis. A wavenumber-dependent shear is produced between the two beams exiting the interferometer. Light exiting the interferometer is collected with an imaging lens that is designed to image the plane of the grating onto the charge-coupled device (CCD). In this configuration, a set of overlapping wavenumber-dependent Fizeau fringes are imaged onto the detector. Only light at the Littrow wavelength will exit parallel to the optical axis, and the generation of ψ, which is the angle the outgoing wavefronts make with the optical axis, is determined by the grating equation:

$$\sigma(\sin\theta_L + \sin(\theta_L - \psi)) = mG \tag{1}$$

where σ is the wavenumber of the incident light, m is the order of diffraction, θ_L is the Littrow angle, and G is the grating groove density. Diffracted by the gratings, the recombining wave fronts exiting the interferometer were crossed. The generation of the spatial frequency of fringes is related to the wavenumber by the equation:

$$f_x = 2\sigma\sin\psi \approx 4(\sigma - \sigma_L)\tan\theta_L, \tag{2}$$

where the approximation assumes small angle ψ and σ_L is the Littrow wavenumber if ψ=0. For the axial rays in one-dimensional SHRS, the input spectral density of $B(\sigma)$ as a function of position x is given by

$$I(x) = \int_0^\infty B(\sigma)\cdot\{1 + \cos[2\pi(4(\sigma - \sigma_L)x\tan\theta_L)]\}d\sigma. \tag{3}$$

where $B(\sigma)$ is the input spectral intensity as a function of wavenumber and x is measured on the detector in the dispersion plane of the diffraction grating. The fringe localization plane was at the gratings, and thus, the gratings were imaged directly on the detector to produce an interferogram. Then the inverse Fourier transform of the interferogram yielded the Raman spectrum.

The maximum theoretical resolving power R of the SHRS was equal to the total resolving power of two diffraction gratings, which is given by

$$R = \frac{\sigma_{\max}}{\delta_\sigma} = 4W\sigma_{\max}\sin\theta_L, \tag{4}$$

where W is the width of diffraction grating and δ_σ is the spectral resolution.

The symmetry of the cosine interferogram in Equation (3) results in folding wavenumbers above and below the Littrow wavenumber ($\sigma_L \pm \Delta\sigma$). In our case, the Littrow wavelength was set to the laser wavenumber; therefore, the Anti-Stokes Raman bands and Stokes Raman bands were overlapped. One way to prevent the unwanted overlap of these two regions is by vertically tilting one of the diffractions by an angle $\varepsilon/2$. The fringes become two-dimensional patterns, and the 2-D interferogram can be rewritten as

$$I(x) = \int_0^\infty B(\sigma)\cdot\{1 + \cos[2\pi(4(\sigma - \sigma_L)x\tan\theta_L) + \sigma y\varepsilon]\}d\sigma. \tag{5}$$

In the field-widened SHRS configuration, the spectral range of one order is limited by the number of samples across the interferometer, which means that the detector pixel numbers limit the spectral range. If the detector has N pixels, the spectral range of the 2-D SHRS is represented by the following equation:

$$\Delta\sigma = N\cdot\delta\sigma. \tag{6}$$

From Equation (6), we can see that the spectral range of the field-widened SHRS is determined by the number of pixels N and the spectral resolution $\delta\sigma$, and the recovered bandpass after 2-D fast Fourier transform is twice that of a 1-D SHRS with the same instrumental parameters.

The SHRS instrument can be field widened by inserting matched dual field-widening prisms between the beamsplitter and each grating shown in Fig. 1. The field-widened prism apex angle and refractive material are chosen so that from a geometrical optics point of view the gratings appear to be coincident. The path different in the system is then near zero for a wide range of input angles and in terms of its angular acceptance. According to the detailed analysis of field widening by Harlander, maximum FoV of the field-widened SHRS system can be achieved by minimizing the quadratic dependence of the phase on the incident angle and use of the prism at minimum deviation with angle of incidence γ given by[12]

$$2\left(n^2-1\right)\tan\gamma = n^2\tan\theta_L \tag{7}$$

where n is the refractive index of the field widening prisms, and the relationship $n\,\sin(\alpha/2) = sin\,\gamma$ determines the prism apex angle α. Setting the Littrow angle equal to 2.305° and the refractive index is 1.527, the apex angle is calculated to be 2.661°.

In the field-widened SHRS system, the field widening prisms improve the resolution by contributing its own resolving power to that of the diffraction grating. The resolving power R is given by

$$R = R_0\left(1-\lambda\frac{dn}{d\lambda}\frac{n}{n^2-1}\right), \tag{8}$$

where R is the correction arising from the dispersion of the prisms with an index of refraction n at wavelength λ.

For a field-widened SHRS system, according to the basic theory of a conventional SHRS system with a shot-noise limit, the SNR can be expressed as[12]

$$\mathrm{SNR} = \sqrt{\frac{\eta A\Omega}{2N} I\,\delta\,\sigma T}, \tag{9}$$

where η is the optical efficiency, A is the effective area of the system, Ω is the etendue of the system, and I is the intensity of the continuum in photons per second per unit area per steradian per unit wavenumber, which is in proportion to the laser power for the measurements. T is the total integration time.

2.2 | Calibration theory

The calibration procedure was based on two known spectral features of two lines from an emission spectrum, such as a mercury lamp.[21] The Littrow wavelength of SHRS can be expressed as

$$\lambda_0 = \frac{f_2 - f_1}{(f_2/\lambda_1)-(f_1/\lambda_2)}, \tag{10}$$

where λ_0 is the Littrow wavenumber, λ_1 and λ_2 are the known wavelengths from the calibration source, and f_1 and f_2 are the measured fringe frequencies of the two known emission lines. Assuming the grating groove density G, the Littrow angle of the diffraction grating is given by Equation (11)

$$\theta_L = arc\sin\left(\frac{\lambda_0\times G}{2}\right). \tag{11}$$

The width of the grating imaged on the detector can be written as

$$W = \frac{f_1}{2(1/\lambda_0 - 1/\lambda_1)\tan(\theta_L)}. \tag{12}$$

Hence, the spectral response of the SHRS can be calculated as

$$\lambda(f) = \frac{\lambda_0\times G}{1-f/(G\times W)}, \tag{13}$$

where f is a measured fringe cycle across the detector width and Equation (13) shows an inverse relationship between the wavelength and the measured fringe cycle.

3 | EXPERIMENTAL

3.1 | Breadboard

Figure 2 shows the layout of the experiment breadboard. The key parameters of all the commercially available, off-the-shelf components used in the experiment breadboard are listed in Table 1. The SHRS was constructed using a 50.8-mm cube beam splitter (Model #: 20BC17MB.1, Newport Opto-Electronics Technologies (Wuxi) Co. Ltd.), two 150 grooves/mm diffraction gratings (Changchun Institute of Optics, Fine Mechanics and Physics,

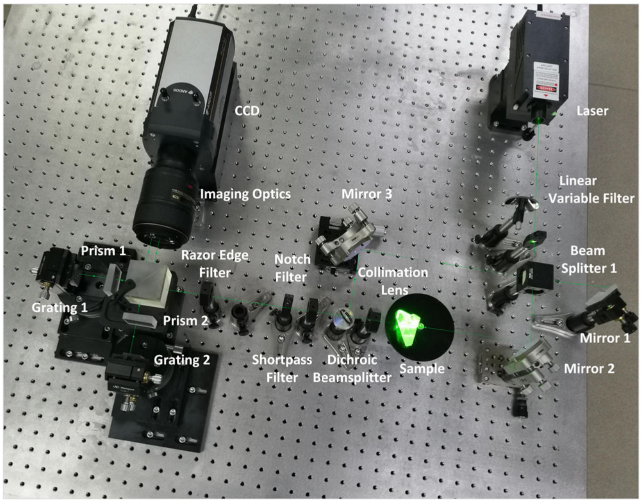

FIGURE 2 The field-widened SHRS breadboard instrument setup [Colour figure can be viewed at wileyonlinelibrary.com]

TABLE 1 The key parameters of the components used in the experiment breadboard

Components	Parameters	Performance index
Laser	Wavelength Beam diameter (1/e, mm) Beam divergence	532 nm, CW ~2.0 <1.5 (full angle, mrad)
Diffraction grating	Groove density Ruled area Blaze angle	150g/mm 13.1×25 mm^2 2.305°
Prism	Apex angle	BK7 2.661°
Beam splitter 2	Size	50.8×50.8×50.8 mm^3
CCD	Pixel numbers Sensor size Pixel size	1,024×1,024 13.3×13.3 nm^2 13×13 μm^2
Laser clean-up filter	Center wavelength FWHM Bandwidth	532 nm 2.0 nm
532 nm Razor Edge long-pass edge Filter	Edge wavelength Transition width Blocking band	536.4 nm 186 cm^{-1} OD_{abs}>6@532 nm
532 nm Razor Edge Dichroic laser-flat Beamsplitter	Edge wavelength Transition width	537.2 nm 186 cm^{-1}
532 nm single- notch Filter	Notch band Blocking band	17 nm OD_{abs}>6@532 nm
700 nm Short pass Filter	Cut-off wavelength Optical density	700 nm ≥4
Imaging optics	Diameter Focal length	62 mm 105 mm

Chinese Academy of Sciences), and two prisms where the apex angle was 2.661° (Changchun UP Optotech (Holding) co., Ltd). The power of the solid state 532-nm green laser could be varied linearly from 0 to 400 mW (Changchun New Industries Optoelectronics Tech. Co., Ltd).

In the experiments, the sample was placed on the focal plane of a 25-mm-diameter collimation lens at a distance of approximately 30 mm from the 532-nm RazorEdge dichroic laser-flat beamsplitter. The angle between the laser beam and the optical axis was 135°, which meant that the dichroic laser-flat beamsplitter reflected the laser line while efficiently transmitting the longer Raman-shifted wavelengths. A 532-nm RazorEdge, long-pass filter (LP03-532RU-25, Semrock) was used to filter out the stray laser light and the Rayleigh-scattered light. The ambient light and fluorescent light at wavelengths longer than 700 nm were filtered out using a 700-nm short-pass filter (84-714, Edmund). In some cases, another 532-nm notch filter (NF01-532U-25, Semrock) was used for laser line rejection. A CCD detector with 1,024×1,024 13-μm pixels (iKon-M 934, Andor) was used to record the fringe image. The CCD was cooled to −60°C to reduce the thermal noise within the sensor chip. One diffraction grating was rotated by a small angle around the *x*-axis. The apex angle of the prism was 2.661°, which was determined by Eq. (7). The Fourier transform of the fringe image was performed by using the fast Fourier transform function. Wavelet threshold function de-noising was adopted to effectively separate the signal from the noise.[22,23]

3.2 | Calibration

We used a mercury lamp for calibration. The three known emission lines of the mercury lamp are 546.075, 576.961, and 579.067 nm. The raw interferogram of the mercury lamp (a), a raw spatial frequency of the mercury lamp (b), and the mercury lamp spectrum from field-widened SHRS (c) are shown in Figure 3. The pixel number of the interferogram is 1,024×1,024.

From Figure 3b, we can see that the primary mercury line 546.075 nm produced 442 fringes across the full width of the detector, the 576.961-nm line produced 240 fringes, and the 579.067-nm line produced 227 fringes. According to Equations (11)–(13), the Littrow wavelength could be calculated to be 536.131 nm, which corresponds to the diffraction grating angle of 2.305°. The width of the grating imaged on the detector could be estimated to be 1.281 cm, and the spectral resolution was 4.853 cm^{-1} and the bandpass was approximately 4,970 cm^{-1}. The breadboard results proved that the calibration results were near to the performance of the SHRS design. The full width at half maximum of the 546.0475-nm line was 5.669 cm^{-1}. This result was in almost exact agreement with the theoretical spectral resolution.

4 | RESULTS AND DISCUSSION

4.1 | Raman spectra analysis of carbon tetrachloride (CCl_4) and SNR analysis

Figure 4 shows that the raw interferograms for carbon tetrachloride are acquired at different laser powers of 108 mW (a), 45 mW (b), and 10 mW (c) with the same integration times of 2 s. At a lower laser power, the interferential fringes are still clearly seen; from the Raman spectra of CCl_4 shown in Figure 4d, the degenerate deformation (T_2) and the symmetric stretching vibrational modes (A_1) are clearly visible at 314 and 459 cm^{-1}, respectively. The third band at 762 cm^{-1} is assigned to the combination mode T_2+A_1. The fourth band at 790 cm^{-1} is assigned to the mode T_1.[24] At the three different laser powers, the signals are still high enough to be

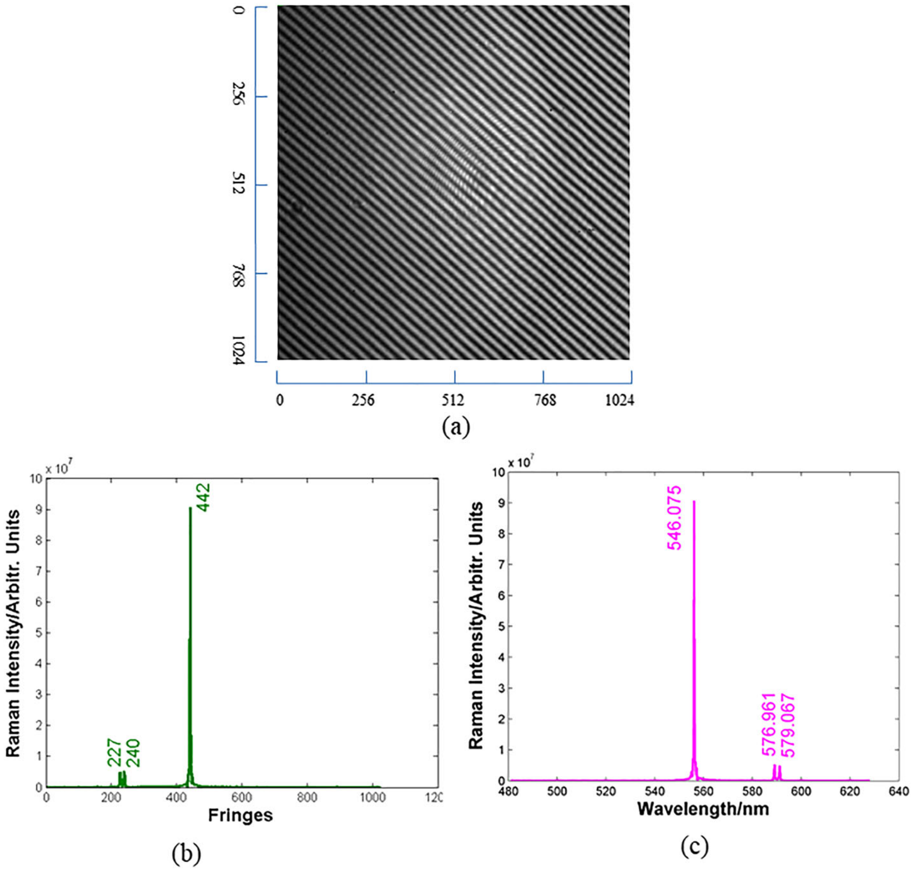

FIGURE 3 (a) Interferogram of the mercury lamp. (b) Raw spatial frequency obtained from 2-D fast Fourier transform. (c) Mercury lamp spectrum as measured after calibration; the absolute line positions are 546.075, 576.961, and 579.067 nm [Colour figure can be viewed at wileyonlinelibrary.com]

identified. We thus observed that the SHRS exhibited excellent sensitivity.

To quantify the performance of the SHRS here, the SNR for the measurement of the Raman spectrum is defined as

$$\mathrm{SNR} = \frac{I_{peak\_signal}}{\mathrm{RMS}_{\mathrm{Noise}}}, \tag{15}$$

where $I_{\mathrm{peak\_signal}}$ is the amplitude at the Raman peak and $\mathrm{RMS}_{\mathrm{Noise}}$ is the root-mean-square (RMS) value of the noise in the spectrum. In our case, the noise is calculated by measuring the RMS in the recovered spectrum of CCl_4. The RMS of the noise is divided by the largest amplitude of the 459/cm Raman peak, which yielded the measured SNR.

To test the stability and repeatability of the system, we measure the SNRs of the field-widened SHRS at different laser powers with an integration time from 2 to 15 s, where the interval time is 1 s, as shown in Figure 5a. We can see that when the laser power was lower than 135 mW, the SNR plots increase with the laser power, which is similar to the plot of the square-root function, then, with a laser power greater than 135 mW, the SNRs decrease a little with the increase of laser power, which was in accordance with Equation (9). Because all the SNR plots show the similar tendency as that in Figure 5a, which shows a good stability and fair repeatability. The SNRs at different integration times with the same laser power of 9 mW are measured only once in Figure 5b. The SNR plot in Figure 5b still coincides with Equation (9).

4.2 | Raman spectral analysis of sulfur

Figure 6 shows the recovered Raman spectra for sulfur at the laser power of 8 mW with the integration time of 0.5 s. Comparing the data collected by an *i*-Raman pro instrument (B&W Tek) with the data collected by our SHRS at the same laser power and same integration time, several differences are observed between the field-widened SHRS spectra after and wavelet threshold denoised and the raw spectra from the *i*-Raman pro instrument. The absolute intensity of Raman peak at 472 cm^{-1} with field widened SHRS is calculated by subtracting the RMS value of noise in the wavenumber range 513-558 cm^{-1} from the intensity of Raman peak at 472 cm^{-1}. The absolute intensity of Raman peak at 472 cm^{-1} with the *i*-Raman pro is calculated by subtracting the RMS

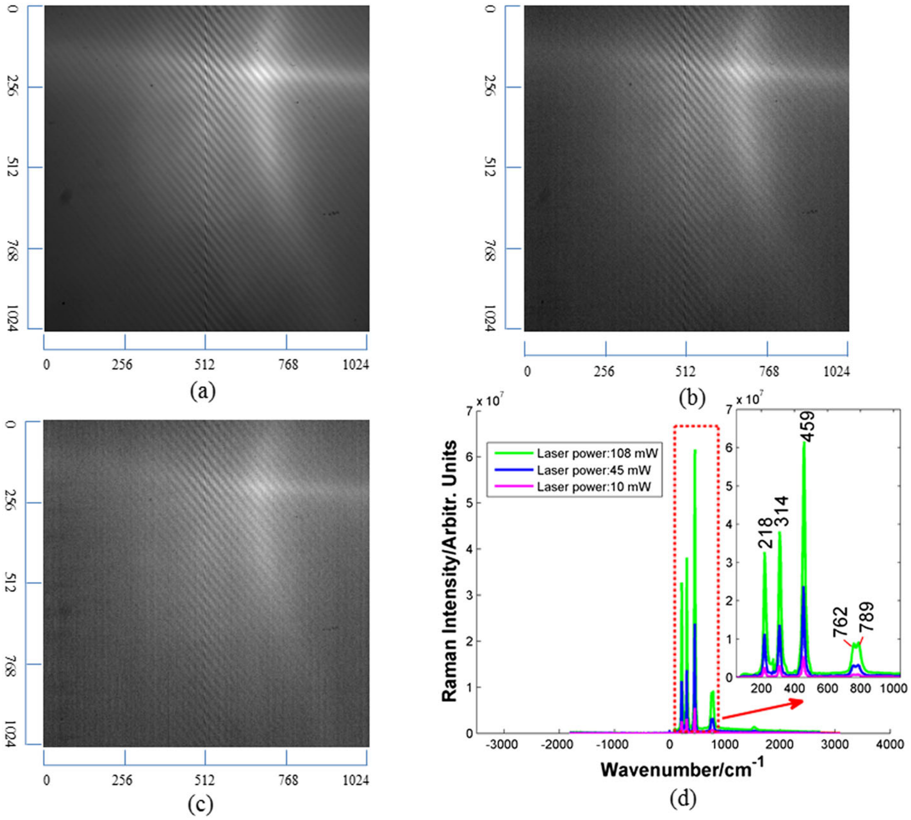

FIGURE 4 (a) Interferogram of CCl_4 at the laser power of 108 mW with an integration time of 2 s. (b) Raw interferogram of CCl_4 at the laser power of 45 mW with the integration time of 2 s. (c) Interferogram of CCl_4 at the laser power of 10 mW with the integration time of 2 s. (d) Recovered Raman spectra of sulfur [Colour figure can be viewed at wileyonlinelibrary.com]

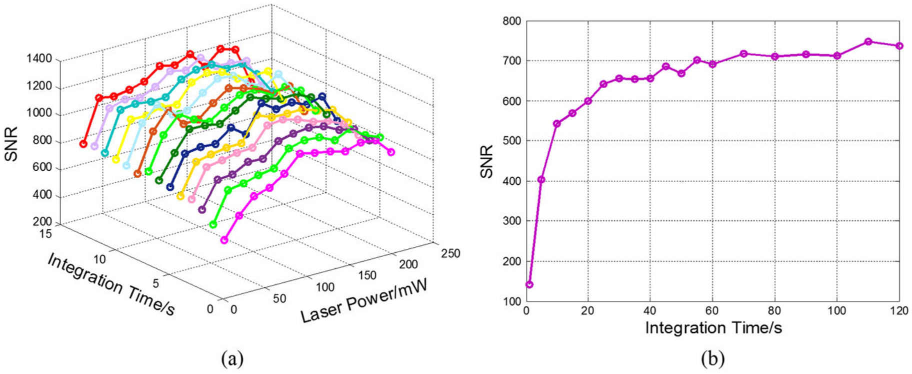

FIGURE 5 (a) Measured signal-to-noise ratio (SNR) at different laser powers with integration times from 2 to 15 s, where the interval time is 1 s. (b) Measured SNR at different integration times with the same laser power of 9 mW [Colour figure can be viewed at wileyonlinelibrary.com]

value of noise in the wavenumber range 509-554 cm^{-1} from the intensity of Raman peak at 472 cm^{-1}. After calculated, the absolute intensity of Raman peak at 472 cm^{-1} with field widened SHRS is 4.544×10^6 and the absolute intensity of Raman peak at 472 cm^{-1} with the *i*-Raman pro is 2.431×10^4. The most obvious difference is that the absolute intensity of the Raman peaks at 472 cm^{-1} is increased by our field-widened SHRS by a factor of approximately 187. This factor can be larger at the 218 cm^{-1} band, but the intensity may be affected by the performance of the filters, because the 218 cm^{-1} band is closer to the Rayleigh scattered light. Therefore, we only adopted the bands far from the Rayleigh line to compare the intensity of the signals. The *i*-Raman Pro is a type of dispersion system. In the B&W system, the divergent and diffuse light is recorded by the detector and can be seen in the spectrum. In the SHRS system, after the divergent light is recombined, there are no fringes on the screen. So, the background has a little influence on our developed system. From the Raman spectra obtained by

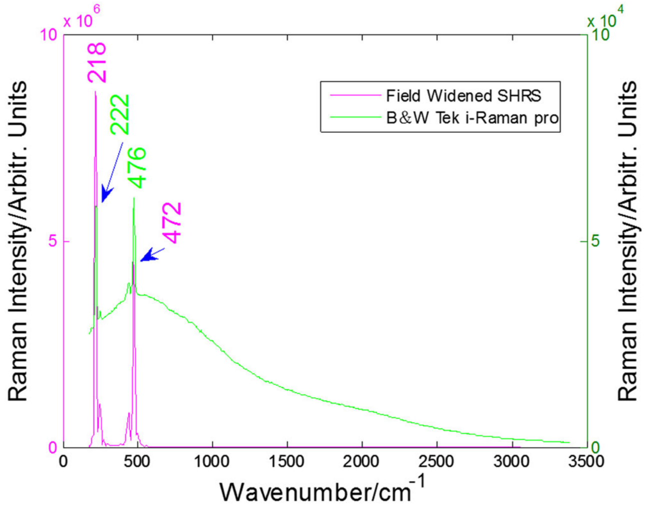

FIGURE 6 Recovered Raman spectra of sulfur at the laser power of 8 mW with the integration time of 0.5 s [Colour figure can be viewed at wileyonlinelibrary.com]

using the commercial Raman instrument, we observe that the background noise and a lower SNR are achieved. In addition, the full width at half maximum of the 218 and 472 cm^{-1} bands are higher using our SHRS. Furthermore, the bandwidth of our SHRS is broader than that of the commercial instrument.

Figure 7 shows the raw interferograms for sulfur (a) and sulfur without field widening (b) at the same laser power of 25 mW with the same integration time of 2 s and the recovered Raman measurements and wide-field measurements for sulfur (c) at the laser power of 25 mW with the integration time of 2 s. The recovered Raman spectra for sulfur and sulfur contained in glass or plastic bottles (d) at the laser power of 25 mW with the integration time of 5 s.

In Figure 7c, the sulfur shows clearly identifiable Raman peaks for both the sulfur and the sulfur contained in a glass or a plastic bottle at the same laser power of 25 mW with the integration time of 5 s. The thickness of the glass bottle is approximately 1.5 mm, and the thickness of the plastic bottle is approximately 2 mm and the main ingredient is high-density polyethylene. The Raman peaks observed at 153 and 218/cm are assigned to the antisymmetric and symmetric bond-bending modes of the S_8 molecule, respectively. The symmetric bond-stretching mode of sulfur appears at 473 cm^{-1}, and the peak at 85/cm is that of the other vibration mode.[25] There is nearly no difference in the spectral resolution between the three spectra of sulfur. Obviously, the SNRs decrease as a result of the laser reflection light from the bottles, but fluorescence from the plastic and degradation

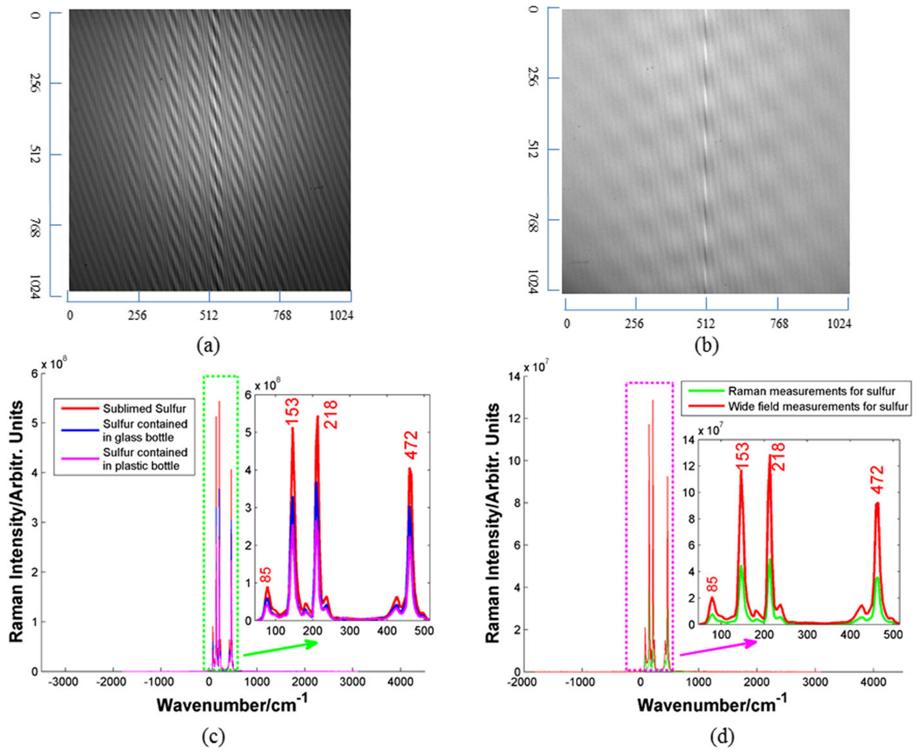

FIGURE 7 (a) Interferogram of sulfur at the laser power of 25 mW with the integration time of 2 s. (b) Interferogram of sulfur at the laser power of 25 mW with the integration time of 2 s without field widening. (c) Recovered Raman spectra of sublimed sulfur and powder sulfur in a glass or in a plastic bag at the laser power of 25 mW with the integration time of 5 s. (d) Recovered Raman measurements and wide-field measurements for sulfur at the laser power of 25 mW with the integration time of 2 s [Colour figure can be viewed at wileyonlinelibrary.com]

is not observed in this experiment. We observe that the field-widened SHRS has the ability to detect samples contained transparent containers, which is very promising for application to practical detections of chemical warfare agents and toxic industrial chemicals that pose a health risk, while not being affected by other factors in the environment.

Figure 7d shows Raman measurement of sulfur and wide-field measurement of sulfur at the same laser power and same integration time. The SNR of the field-widened SHRS is 918, and the SNR of conventional SHRS is 355 with the same instrumental parameters. Compared with the SHRS without field widening, the spectrum is improved by a factor of 2.58.

4.3 | Raman spectral of sodium sulfate in solid state and in aqueous solution

Figure 8 shows the raw interferograms of solid sodium sulfate (Na_2SO_4) (a) and Na_4SO_4 (0.7 mol/L) in aqueous solution (b) at the same laser power of 135 mW with the same integration time of 3 s; the recovered Raman spectra of solid Na_2SO_4 are shown in Figure 7c; the recovered Raman spectra of Na_2SO_4 in aqueous solution (0.7 mol/L, 0.45 mol/L) are shown in Figure 8d. The main Raman peak at 992 cm^{-1} is assigned to the $\nu_1(A_1)$ mode. The ν_2 and ν_4 modes are detected in the low wavenumber region, and the ν_3 mode is in the high wavenumber region.[26] After magnification, the weak Raman peaks could be clearly seen in the spectrum, as shown in Figure 8b. We compare the Raman spectra of Na_2SO_4 in aqueous solution at two molarities (0.7 and 0.45 mol/L). The symmetric stretching ν_1 is clearly discernible in the Raman spectra of Na_2SO_4 in aqueous solution. The characteristic OH vibrations, as the bending mode at approximately 1,633 cm^{-1} is present. The detection capabilities of the SHRS demonstrate in this work are very promising for applications in geochemistry and environmental measurements.

4.4 | Raman spectral analysis of a mixture of organic liquids and inorganic solids

Figure 9a shows the Raman spectra of acetone, cyclohexane, carbon tetrachloride, and a mixture of the three organic liquids. In the spectra of acetone, cyclohexane, and carbon tetrachloride, the main Raman peaks are well detected. Because of the different intensities of the three organic liquids, the 531, 787, 1,222, 1,710, and 2,922cm^{-1} peaks of acetone; the 803, 1,029, 1,267, 1,444,

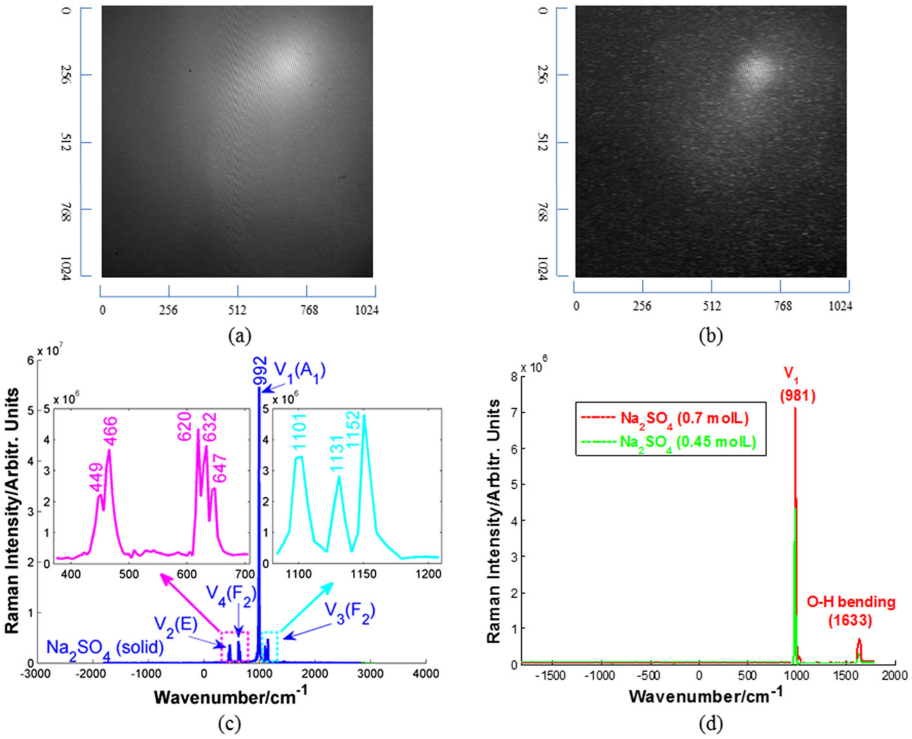

FIGURE 8 (a) Interferogram of solid Na_2SO_4 at the laser power of 135 mW with the integration time of 3 s. (b) Raw interferogram of Na_2SO_4 (0.7 mol/L) in aqueous solution at the laser power of 135 mW with the integration time of 3 s. (c) Recovered Raman spectra of solid Na_2SO_4. (d) Recovered Raman spectra of Na_2SO_4 in aqueous solution (0.7 mol/L, 0.45 mol/L) [Colour figure can be viewed at wileyonlinelibrary.com]

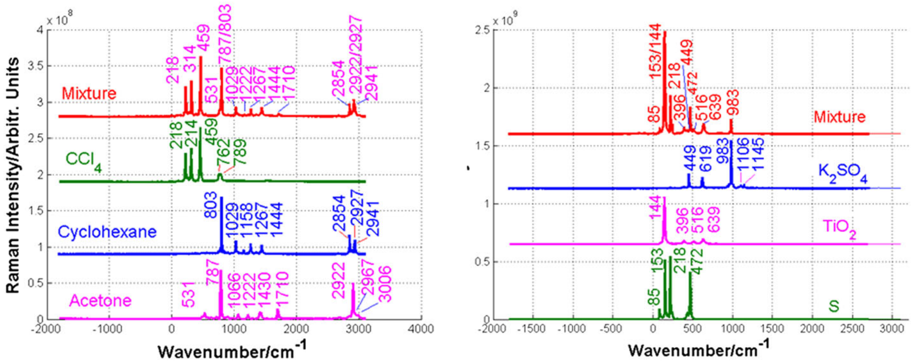

(a) (b)

FIGURE 9 (a) Raman spectra of organic liquids with a laser power of 108 mW and integration time of 5 s. (b) Raman spectra of inorganic solids with a laser power of 108 mW and an integration time of 6 s [Colour figure can be viewed at wileyonlinelibrary.com]

2,854, 2,927, and 2,941cm^{-1} peaks of cyclohexane; and the 218, 314, 459, and 789 cm^{-1} peaks of carbon tetrachloride could be distinguished in the Raman spectrum of the mixture of the three organic liquids. In the spectrum of the mixture, most of the Raman signals are observed. The results prove that not only does the field-widened SHRS have a broad bandpass but also the SNR is high enough to distinguish weak Raman signals.

Figure 9b shows the Raman spectra of sulfur, titanium dioxide, and potassium sulfate. In the Raman spectra of the pure solids, the Raman peaks are clearly visible. The main Raman peaks of the pure solids are also well visualized in the Raman spectrum of the mixture of the three solids.

4.5 | Raman spectral analysis of rocks

Figure 10 shows the Raman spectra of celestine, calcite, and rose quartz. In celestine ($SrSO_4$), the Raman peaks located at 1,001, 459, 1,111/1,158, and 622/659cm^{-1} correspond to the nondegenerate symmetric stretching vibration mode ν_1, doubly degenerate deformation vibration mode ν_2, triply degenerate stretching vibration mode ν_3, and the triple bending vibration mode ν_4, respectively, which are in good agreement with previous work.[27] For calcite ($CaCO_3$), an intense sharp Raman band at 1,085cm^{-1} is assigned to the $\nu_1(CO_3)^{2-}$ symmetric stretching mode. The $\nu_4(CO_3)$ bending mode is clearly visible at 711cm^{-1}.[28] The lattice modes of calcite at 155 and 282/cm could also be distinguished. The main Raman peaks of rose quartz are also easily distinguished. The results from these three rocks clearly show that the SHRS is capable of capturing the weak Raman signals from these minerals.

4.6 | Stokes and anti-Stokes band detection

Figure 11 shows the Stokes and anti-Stokes Raman spectra of carbon tetrachloride (a) and sulfur (b) that are recorded at room temperature. To test the anti-Stokes band, the edge filter is replaced with a 532-nm notch filter to limit the pass band and minimize noise. In the Stokes region (right of the band) and anti-Stokes region (left of the band), the Raman shifts at 472cm^{-1} for sulfur, as well as at 459 and 762/789cm^{-1} for CCl_4 could be seen without overlap. According to the Maxwell–Boltzmann law, a larger Raman shift is accompanied by a smaller ratio. Therefore, to detect a larger anti-Stokes Raman shift, a higher SNR of the SHRS is required by field widening.

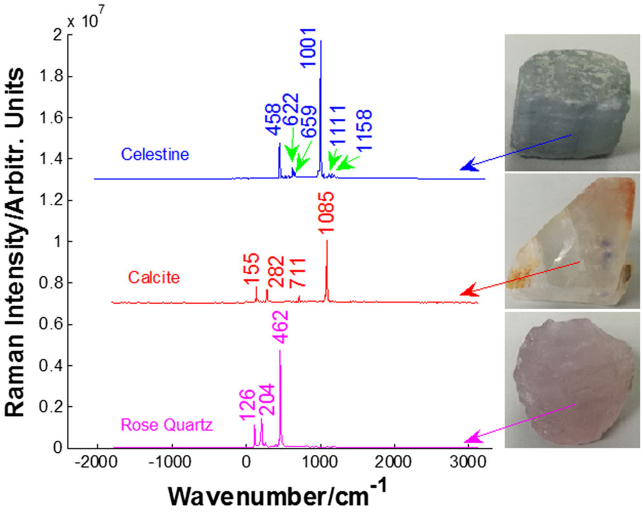

FIGURE 10 Raman spectra of three rocks: rose quartz, calcite, and celestine at the laser power of 25 mW with the same integration time of 5 s [Colour figure can be viewed at wileyonlinelibrary.com]

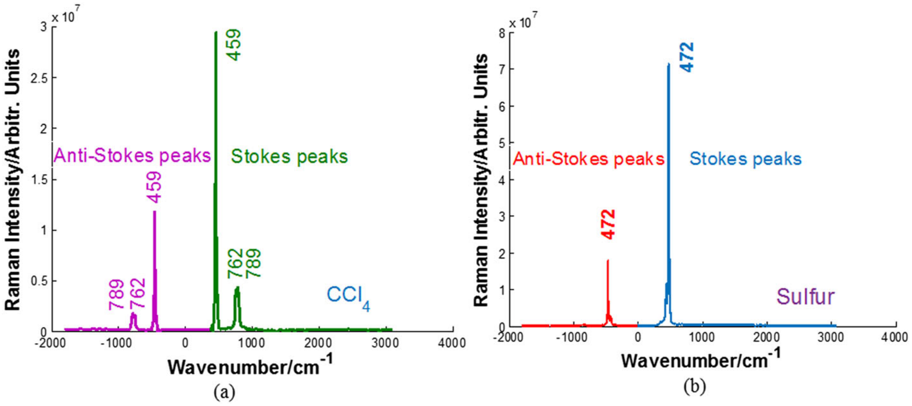

(a)

(b)

FIGURE 11 (a) Raman spectra of CCl_4 at the laser power of 45 mW with the integration time of 2 s. (b) Raman spectra of sulfur at the laser power of 99 mW with the integration time of 1 s [Colour figure can be viewed at wileyonlinelibrary.com]

5 | CONCLUSIONS

In this paper, a field-widened SHRS breadboard has been designed and built. In the experiments, we demonstrated that the field-widened SHRS exhibits a good stability and fair repeatability by measuring the SNR of carbon tetrachloride with different integration times and laser powers. A commercial Raman instrument and the field-widened SHRS were compared, and a higher spectral resolution, a broader bandwidth, and higher SNR could be achieved by our SHRS. Furthermore, from a comparison of the Raman spectra of sulfur detected by the field-widened SHRS and a SHRS of the same instrumental parameters without field widening, the application of the field widening by prisms is useful to improve the SNR of the recovered Raman spectra. We believe that the field-widened SHRS has an enhanced detection capability owing to factors such as sensitivity, response time, and low laser power requirements and will be used under hazardous and complex environments. We were able to measure targets in containers, which is very important for detecting toxic targets that should not be exposed; this is the first time that it has been possible to measure the Raman spectra of sodium sulfate in the solid state and in aqueous solution with a field-widened SHRS. The field-widened SHRS is able to separate targeted compounds by testing the mixture of organic liquids or inorganic solids. We demonstrated the field-widened SHRS' ability to detect Raman spectra of minerals and anti-Stokes bands. The wide-field detections do not require long integration times or high laser powers without loss of sensitivity or spectral resolution and are therefore very promising for planetary science applications.

ORCID

Jun Qiu https://orcid.org/0000-0002-4822-7736

REFERENCES

[1] L. Zhang, R. Yang, X. Liu, F. Han, K. Evans-Lutterodt, H. Wang, Y. He, J. Wang, Y. Zhao, W. Yang, *Light-Sci Appl.* **2018**, *8*, 4558.

[2] H. Lin, C. S. Liao, P. Wang, J. X. Cheng, *Light-Sci Appl.* **2018**, *7*, 17179.

[3] L. S. Fan, L. Constanin, D. W. Li, L. liu, K. Keramatnejad, C. Azina, X. Huang, H. R. Golgir, Y. Lu, Z. Ahmadi, F. Wang, J. Shield, B. Cui, J. F. Silvain, Y. F. Lu, *Light-Sci Appl.* **2018**, *7*, 17177.

[4] E. C. Cull, M. E. Gehm, B. D. Guenther, D. J. Brady, *Proc. SPIE* **2005**, *5994*, 233.

[5] T. Steinle, V. Kumar, M. Floess, A. Steinmann, M. Marangoni, C. Koch, C. Wege, G. Cerullo, H. Giessen, *Light-Sci Appl.* **2016**, *5*, 16149.

[6] A. Novelli-Rousseau, I. Espagnon, D. Filiputti, O. Gal, A. Douet, F. Mallard, Q. Josso, *Light-Sci Appl.* **2018**, *8*, 3957.

[7] S. Mattana, M. Mattarelli, L. Urbanelli, S. Krizia, E. Carla, D. S. Mauro, F. Daniele, C. Silvia, *Light-Sci Appl.* **2018**, *7*, 17139.

[8] H. Wang, M. A. Boraey, L. Williams, D. Lechuga-Ballesteros, R. Vehring, *Int. J. Pharm.* **2014**, *469*, 197.

[9] A. K. Misra, S. K. Sharma, C. H. Chio, P. G. Lucey, B. Lienert, *Spectrochim. Acta. A.* **2005**, *61*, 2281.

[10] J. D. Stopar, P. G. Lucey, S. K. Sharma, A. K. Misra, G. J. Taylor, H. W. Hubble, *Spectrochim. Acta A.* **2005**, *61*, 2315.

[11] B. Fazio, P. Artoni, M. A. Iatì, C. D'Andrea, M. J. Lo Faro, S. D. Sorbo, S. Pirotta, P. G. Gucciardi, P. Musumeci, C. S.e. Vasi, R. Saija, M. Galli, F. Priolo, A. Irrera, *Light-Sci Appl.* **2016**, *5*, 16062.

[12] J. M. Harlander, “Spatial heterodyne spectroscopy: interferometric performance at any wavelength without scanning,” Thesis (Ph.D.) University of Wisconsin—Madison, **1991**.

[13] N. Lamsal, S. M. Angle, *Appl. Spectrosc* **2015**, *69*(5), 525.

[14] N. Lamsal, S. M. Angle, S.K. Sharma, T.E. Acosta, 46th Lunar and Planetary Science Conference **2015**.

[15] G. Hu, W. Xiong, H. Shi, Z. Li, J. Shen, X. Fang, *Opt. Eng* **2015**, *54*, 114101.

[16] G. Hu, W. Xiong, H. Luo, H. Shi, Z. Li, J. Shen, X. Fang, B. Xu, J. Zhang, *Appl. Spectrosc* **2018**, *72*, 151.

[17] M. J. Foster, J. Storey, M. A. Zentile, *Opt. Express.* **2017**, *25*, 1598.

[18] J. Harlander, H. T. Tran, F. L. Roesler, K. Jaehnig, S. M. Seo, W. Sanders, R. J Reynolds, SPIE's 1994 International Symposium on Optics, Imaging, and Instrumentation. International Society for Optics and Photonics, **1994**.

[19] D. D. Gardner, E. J. Mierkiewicz, F. L. Roesler, J. M. Harlander, K. P. Jaehnig, S. M. Nossal, L. M. Haffner, *J. Geophys Res-Space.* **2017**, (1), 122.

[20] C. N. Pannell, B. G. Zhang, M. K. Reed, Proc. SPIE, Photonic Instrumentation Engineering II, **2015**,936903.

[21] C. R. Englert, J. M. Harlander, J. C. Owrutsky, J. T. Bays, *Nav. Res. Lab.* **2005**, NRL/MR/7640-05-8926, 1.

[22] M. Misiti, Y. Misiti, G. Oppenheim, J. M. Poggi, *Wavelet Toolbox User's Guide*, The Math Works, Inc **2018** 60.

[23] Jun. Q, X. Qi, X. Li, Z. Ma, Jirigalantu, Y. Tang, X. Mi, X. Zheng, R. Zhang, and Bayanheshig, *Opt. Express.* **2018**, *26*, 11994.

[24] David Tuschel, *Spectroscopy* **2014**, *29*(3), 15.

[25] J. Lin, Y. Li, *Opt Lett* **2014**, *39*(1), 108.

[26] B. M. Kawther, H. K. Thomas, A. Hassen, D. F. Marc, *J. Raman. Spectrosc* **2013**, *44*, 1603.

[27] Y. H. Chen, S. C. Yu, E. Huang, *Physica. B* **2010**, *405*(20), 4386.

[28] J. Sun, Z. Wu, H. Cheng, *Spectochim. Acta. A* **2014**, *117*, 158.

How to cite this article: Qiu J, Qi X, Li X, et al. Raman measurements using a field-widened spatial heterodyne Raman spectrometer. *J Raman Spectrosc*. 2019;1–12. https://doi.org/10.1002/jrs.5659